Benchmarking Turbulence Models to Represent Cloud-Edge Mixing

Benchmarking Turbulence Models to Represent Cloud-Edge Mixing

JOHANNES KAINZ,[a] NIKITABAHEN N. MAKWANA,[b] BIPIN KUMAR,[b] S. RAVICHANDRAN,[c] JOHAN FRIES,[d] GAETANO SARDINA,[e] BERNHARD MEHLIG,[d,e] AND FABIAN HOFFMANN[f]

[a] *Ludwig-Maximilians-Universität München, Munich, Germany*
[b] *Indian Institute of Tropical Meteorology, Pune, India*
[c] *Centre for Climate Studies, Indian Institute of Technology Bombay, Mumbai, India*
[d] *Gothenburg University, Gothenburg, Sweden*
[e] *Chalmers University of Technology, Gothenburg, Sweden*
[f] *Freie Universität Berlin, Berlin, Germany*

(Manuscript received 14 October 2024, in final form 24 February 2026, accepted 11 March 2026)

ABSTRACT: Considering turbulence is crucial to understanding clouds. However, covering all scales involved in the turbulent mixing of clouds with their environment is computationally challenging, urging the development of simpler models to represent some of the processes involved. By using full direct numerical simulations as a reference, this study compares several statistical approaches for representing small-scale turbulent mixing, while assessing their applicability as subgrid-scale models for large-eddy simulations. All models use a comparable Lagrangian representation of cloud microphysics and simulate the same cases of cloud-edge mixing, covering different ambient humidities and turbulence intensities. It is demonstrated that all statistical models represent the evolution of thermodynamics successfully, but not all models capture the changes in cloud microphysics (cloud droplet number concentration, droplet mean radius, and spectral width). Accurate microphysical evolution arises when the modeling framework represents spatially heterogeneous supersaturation and its time evolution along mixing interfaces, either by explicitly resolving turbulence or by evolving the full probability distribution of the scalar. Models that relax toward a space-dependent mean recover key features such as spatial asymmetry and partial broadening and, therefore, constitute a useful representation of mixing under carefully chosen circumstances. By comparison, models relying on a space-independent mean systematically compress the distribution. These results identify the representation of supersaturation variability and its history as the primary requirement for representing small-scale mixing in clouds.

SIGNIFICANCE STATEMENT: Although small-scale turbulence is crucial to the development of clouds, the representation of its effects is challenging. Direct numerical simulations accurately represent the underlying fluid dynamics and cloud microphysical processes on all relevant length and time scales but require enormous computational resources. Therefore, simplified models are used to parameterize the effects of small-scale turbulence on clouds. Here, we compare four approaches of different complexities to the results from direct numerical simulations. While simpler models successfully capture changes in thermodynamic quantities, the adequate consideration of spatial dependencies is shown to be necessary to represent the development of cloud droplets.

KEYWORDS: Turbulence; Cloud droplets; Cloud microphysics; Cloud parameterizations; Clouds; Subgrid-scale processes

1. Introduction

Today, although considerable progress has been made in understanding Earth's climate system, the role of clouds still raises questions. One reason for this lack of understanding is that clouds are a multiscale and multiprocess system, ranging from the large-scale organization of cloud fields (~100 km) to the smallest scales of turbulence (~1 mm), with which aerosols, cloud droplets, and precipitation interact (~1–1000 μm) (Bodenschatz et al. 2010).

Due to computational constraints, most modeling of the atmosphere focuses on scales larger than 100 m, while smaller-scale processes are parameterized. One of these processes is the mixing of cloudy and cloud-free air (Baker and Latham 1979), which can change the cloud microphysical composition and, hence, the role of clouds in Earth's radiation budget (Hoffmann 2023). The mixing is termed homogeneous if the liquid water mixing ratio (q_c) decreases by evaporating all cloud droplets partially, that is, reducing their size but not their number concentration (N_c). During extreme inhomogeneous mixing, q_c is reduced by evaporating individual droplets completely, while leaving others unblemished. Thus, N_c decreases but not the mean droplet size. It is important to note that in both cases, N_c must eventually decrease by the dilution caused by the mixing with entrained air.

In nature, mixing is usually constrained to the interface of cloudy filaments reaching into subsaturated air. If this filament is not resolved by the model, mixing becomes instantaneous and affects all droplets located in a model grid box simultaneously, which forces mixing to be preferentially homogeneous (e.g.,

Denotes content that is immediately available upon publication as open access.

Corresponding author: Fabian Hoffmann, f.hoffmann@fu-berlin.de

DOI: 10.1175/JAS-D-24-0228.1

Kainz and Hoffmann 2023). Direct numerical simulations (DNSs), which represent all relevant scales of small-scale turbulence, may be applied to study cloud-edge mixing but are constrained to small domains of up to a meter due to the commensurately large computational requirements (Kumar et al. 2012, 2013, 2014). To address larger scales, large-eddy simulations (LESs) are commonly applied, which avoid high spatial and temporal resolutions by representing dynamics only on scales larger than tens to hundreds of meters, while parameterizations are used to consider the effects of unresolved scales on the resolved flow (Smagorinsky 1963; Deardorff 1980). A key challenge is that unresolved turbulence not only affects the dynamics, and other parameterizations are necessary to represent, for instance, the effect of turbulent water vapor supersaturation fluctuations on the condensational growth of cloud droplets (e.g., Hoffmann and Feingold 2019).

In this study, we compare different statistical turbulence models and investigate how well they describe the condensation and evaporation of cloud droplets during the mixing of cloudy and cloud-free air. We consider three supersaturation fluctuation models (Pope 1994): The first one is an iteration of the interaction-by-exchange-with-the-mean (IEM) model (Villermaux 1986; Pope 1994; Grabowski and Abade 2017; Abade et al. 2018), which considers stochastic supersaturation fluctuations relaxing to a space-independent (i.e., domain-averaged) mean, making it one of the simplest models of scalar mixing (Pozorski and Waclawczyk 2020). The second model approximates supersaturation fluctuations by relaxation to a space-dependent mean [relaxation-to-mean model (RMM)] (Pope 2000; Fries et al. 2021). The third model rests on the mapping-closure approximation [mapping-closure model (MCM)], considering even more space-dependent dependencies (Chen et al. 1989; Pope 1991; Fries et al. 2023). In addition to the supersaturation fluctuation models, we also analyze the one-dimensional linear eddy model (LEM) (Kerstein 1988), which represents the evolution of supersaturation by predicting the relocation of scalars through a statistical approach. The LEM and IEM have already been used to represent subgrid-scale supersaturation fluctuations in LESs (Hoffmann and Feingold 2019; Chandrakar et al. 2021). Fries et al. (2021) employed the RMM to estimate the degree of inhomogeneous mixing in the data of Beals et al. (2015). The MCM was benchmarked against a DNS of Kumar et al. (2012).

Until now, there have been no systematic studies comparing the strengths and weaknesses of the IEM, RMM, MCM, and LEM. Thus, in the present study, we

- compare all models mentioned above against each other and with a set of new reference DNSs based on Kumar et al. (2014),
- test to which extent the models describe the thermodynamical and cloud microphysical responses to different turbulence intensities and ambient humidities, and
- discuss aspects necessary to consider when the different approaches are used as subgrid-scale models in LESs.

The paper is organized as follows. First, each model is introduced, and the case setups are presented. Then, two sensitivity studies, one assessing the effect of turbulence intensity and one assessing the effect of ambient humidity, are discussed. Differences between the models are highlighted, and the applicability of the models as subgrid-scale schemes is discussed. We then conclude with remarks on future work.

2. Models

The main way cloud microphysics and dynamics interact is through supersaturation, which drives the condensation and evaporation of cloud droplets. The relative supersaturation can be defined as

$$S(\mathbf{x}, t) = \frac{q_v(\mathbf{x}, t)}{q_{vs}[T(\mathbf{x}, t), p]} - 1 \tag{1}$$

and is determined by the water vapor mixing ratio q_v and absolute temperature T, where q_{vs} is the saturation water vapor mixing ratio over liquid water and p is the hydrostatic pressure. Fundamentally, S is a field, defined at any point in space $\mathbf{x}$ and time t. Supersaturation fluctuations are shaped by the advection of q_v and T, as well as sinks and sources, e.g., the condensation and evaporation of cloud droplets.

All models used in this study aim to determine the spatial and temporal fluctuations of S. The most fundamental approach is DNS, described first, followed by short introductions to the LEM, IEM, RMM, and MCM, which idealize the underlying processes to different degrees. Note that the following descriptions cannot provide the depth necessary to understand each approach completely. Thus, references are given to guide the interested reader to further information.

a. DNS

DNSs are the most accurate approach to investigate the dynamics of fluids (Moin and Mahesh 1998) and have been adapted to investigate clouds in the last decades (e.g., Vaillancourt et al. 2001). The applied DNS model is described in Kumar et al. (2013, 2014, 2017). To predict the velocity of air $\mathbf{u}$, where bold font indicates a three-dimensional vector, the DNS solves the incompressible, Oberbeck–Boussinesq-approximated Navier–Stokes equations. These are

$$\frac{\partial \mathbf{u}}{\partial t} + (\mathbf{u}\cdot\boldsymbol{\nabla})\mathbf{u} = -\frac{1}{\rho_0}\nabla p + \nu\boldsymbol{\nabla}^2\mathbf{u} + \mathbf{B} + \mathbf{f}_{\mathrm{LS}}, \tag{2}$$

where $\boldsymbol{\nabla}$ and $\partial/\partial t$ denote the spatial and temporal derivatives, ρ_0 is a reference air density, ν is the kinematic viscosity of dry air, $\mathbf{B}$ is the buoyancy force [Eq. (6) in Kumar et al. (2014)], and $\mathbf{f}_{\mathrm{LS}}$ is a large-scale forcing driving the flow in a statistically stationary fashion [Eq. (7) in Kumar et al. (2014)].

The thermodynamic fields T and q_v obey

$$\frac{\partial T}{\partial t} + \mathbf{u}\cdot\boldsymbol{\nabla}T = D_\kappa\boldsymbol{\nabla}^2T + \frac{l_v}{c_p}C_d, \tag{3a}$$

$$\frac{\partial q_v}{\partial t} + \mathbf{u}\cdot\boldsymbol{\nabla}q_v = D_v\boldsymbol{\nabla}^2q_v - C_d, \tag{3b}$$

where D_κ is the molecular diffusivity of heat, D_v is the molecular diffusivity of water vapor, l_v is the enthalpy of vaporization, and

c_p is the specific heat of air at constant pressure. The effect of condensation and evaporation on T and q_v in Eq. (3) is considered by

$$C_d(\mathbf{x}, t) = \frac{4}{3}\pi\frac{\rho_l}{\rho_0}\sum_{\alpha}^{N}\frac{G(\mathbf{x} - \mathbf{x}_\alpha; \Delta V)}{\Delta V}\frac{dr_\alpha^3}{dt}. \tag{4}$$

Here, $\mathbf{x}$ is a location vector and $\mathbf{x}_\alpha$ is the location of a cloud droplet α, where radius growth rate by condensation is dr_α/dt. The number of all droplet is given by N. The ρ_l is the density of liquid water. The spatial kernel G is unity in a volume ΔV around $\mathbf{x}$, and zero otherwise. For DNS, ΔV is identical to the volume of a DNS grid cell.

Note that our case has no imposed mean stratification or mean updraft. Thus, vertical velocity fluctuations influence T and q_v only through the advective terms $\mathbf{u} \cdot \boldsymbol{\nabla}$ in Eq. (3), and no explicit updraft forcing appears in here and in the subsequently described models.

Cloud droplet dynamics are described in a Lagrangian fashion, as heavy spherical inertial particles (Bec et al. 2024). In the Stokes approximation, their equations of motion read

$$\frac{d\mathbf{x}_\alpha}{dt} = \mathbf{v}_\alpha, \tag{5a}$$

$$\frac{d\mathbf{v}_\alpha}{dt} = \frac{1}{\tau_s}[\mathbf{u}(\mathbf{x}_\alpha) - \mathbf{v}_\alpha] - \mathbf{g}, \tag{5b}$$

where $\mathbf{v}_\alpha$ is the droplet velocity and $\mathbf{u}(\mathbf{x}_\alpha)$ is the air velocity at the droplet's location. The term $\mathbf{g}$ describes the acceleration due to gravity. The influence of drag is considered by the particle response time in Stokes approximation, $\tau_s = 2\rho_l r_\alpha^2/(9\rho_0\nu)$, where r_α is the radius of the considered droplet.

The change in droplet radius due to evaporation and condensation is modeled as

$$r_\alpha\frac{dr_\alpha}{dt} = KS(\mathbf{x}_\alpha, t), \tag{6}$$

which is primarily driven by S determined from T and q_v via Eq. (1) at $\mathbf{x}_\alpha$. The growth rate is scaled by $K = 1/[\rho_l(K_D + K_\kappa)]$, with $K_D = R_v T/[e_s(T)D_v]$ considering the molecular diffusion of water vapor and $K_\kappa = [l_v/(R_v T) - 1]l_v/(\kappa T)$ considering the conduction of heat. Here, R_v is the gas constant of water vapor, $e_s(T)$ is the saturation vapor pressure, and κ is the thermal conductivity of air.

b. LEM

The LEM is a statistical turbulence model developed by Kerstein (1988) and was introduced to cloud physics by Krueger (1993). The implementation used in this study follows Hoffmann (2020). The LEM deviates from DNS by utilizing a one-dimensional description of inertial-range turbulence, in terms of an idealized mapping approach.

As such, the model does not predict the turbulent fluid velocity but directly prescribes the relocation of scalars as

$$T(x, t + dt) = T[M(x), t], \tag{7a}$$

$$q_v(x, t + dt) = q_v[M(x), t]. \tag{7b}$$

The mapping M mimics turbulent stretching and folding, i.e., it steeps gradients in T and q_v, with the exact mathematical treatment shown in, e.g., Eq. (10.2) by Menon and Kerstein (2011). The M is applied with a probability of $\Delta t/\tau_{\mathrm{LEM}}$, with Δt being the model time step and τ_{LEM} being the average time between two turbulent eddies mixing the domain. The τ_{LEM} is determined from inertial range scaling using the outer scale of turbulence L and the kinetic energy dissipation rate ε, as well as the domain size L_x [Eq. (2.4) in Krueger (1993)]. The M places an eddy at a random location in the domain, and its size l is randomly chosen from the spectrum of eddy lengths in the inertial subrange, bounded by L_{outer} and the Kolmogorov length scale η [Eq. (2.3) in Krueger (1993)], which describes the smallest scale of motion in the flow. Below this scale, molecular diffusion is the dominant driver of energy dissipation.

The evolution of T and q_v by molecular diffusion and condensation is described by

$$\frac{\partial T}{\partial t} = D_\kappa\frac{\partial^2 T}{\partial^2 x} + \frac{l_v}{c_p}C_d, \tag{8a}$$

$$\frac{\partial q_v}{\partial t} = D_v\frac{\partial^2 q_v}{\partial^2 x} - C_d. \tag{8b}$$

Compared with the DNS, Eqs. (3) and (8) miss the advection term on their left-hand sides, which is considered in the LEM via M in Eq. (7). Note that although the LEM is one-dimensional by design, its grid boxes are three-dimensional to represent droplet-concentration-dependent processes correctly. Thus, C_d is evaluated as in the DNS with the reference volume matching the volume of a LEM grid box.

It is assumed that cloud droplets move with the surrounding fluid. Thus, their location changes as

$$x_\alpha(t + dt) = x[M(x_\alpha)], \tag{9}$$

utilizing the same mapping considered in Eq. (7). While this is a simplification the following models heavily rely on, it is not a necessary requirement for the LEM, in which it is possible to consider sedimentation or inertia effects that could decouple the motion of droplets from the motion of the fluid (Krueger and Kerstein 2018). These effects are neglected in the present study.

Droplet condensational growth is determined as

$$r_\alpha\frac{dr_\alpha}{dt} = KS(x_\alpha). \tag{10}$$

Similar to DNS, S is determined from T and q_v via Eq. (1), but at x_α, the droplet's location in one-dimensional space. This constitutes a minor difference to DNS, where S is evaluated in three-dimensional space.

c. IEM

Our implementation of the IEM is based on a statistical model originally suggested by Villermaux (1986) with further descriptions in Borghi (1988) and Pope (1994). In a cloud microphysical context, the IEM was applied by Grabowski and

Abade (2017) and Abade et al. (2018) for studying the broadening of droplet size distributions through vertical velocity fluctuations. The model was improved by Saito et al. (2021), who reduced the number of model variables, while keeping the capability to reproduce the scaling of the model parameters unchanged.

In the IEM's original formulation, the composition of Lagrangian fluid elements (e.g., their supersaturation) relaxes toward a space-dependent mean. In this study, however, we use a space-independent mean, similar to the IEM-based LES subgrid-scale model by Chandrakar et al. (2021). In the following subsection, we also discuss the RMM, which uses a space-dependent mean and is, therefore, closer to the IEM's original formulation, but might impede the application as an LES subgrid-scale model, as discussed in section 5a.

The IEM solves prognostic equations for the domain-averaged T and q_v as

$$\frac{\partial \overline{T}}{\partial t} = \frac{l_v}{c_p} C_d, \tag{11a}$$

$$\frac{\partial \overline{q_v}}{\partial t} = -C_d, \tag{11b}$$

where $\overline{(..)}$ indicates the domain average. Because $\overline{T}$ and $\overline{q_v}$ are domain-averaged quantities, advection and molecular diffusion are not considered, and the reference volume to determine C_d encloses the entire domain. From $\overline{T}$ and $\overline{q_v}$, the desired $\overline{S}$ is determined via Eq. (1).

A perturbation from $\overline{S}$ is predicted for Lagrangian fluid elements by

$$\frac{dS'_\alpha}{dt} = -C_{\mathrm{IEM},1}\frac{S'_\alpha}{\tau_L} - C_{\mathrm{IEM},2}\frac{S'_\alpha}{\tau_p}, \tag{12}$$

and it is assumed that cloud droplets move with those fluid elements. The first term represents changes in S'_α due to turbulent mixing, steered by the integral time scale of turbulence:

$$\tau_L = \left(\frac{L^2_{\mathrm{outer}}}{\varepsilon}\right)^{1/3}.$$

The second term depicts changes due to condensation or evaporation by S'_α and is derived from C_d. The rate of condensation or evaporation is the phase relaxation time scale:

$$\tau_p = \frac{1}{a_S a_K r_m N_c},$$

which is determined from the average droplet radius r_m and the domain-averaged droplet concentration mixing ratio N_c, with $a_S = [1/q_v + l_v^2/(c_p R_v T^2)]$ and $a_K = 4\pi\rho_l K$. Note that the parameters $C_{\mathrm{IEM},1}$ and $C_{\mathrm{IEM},2}$ are tuning parameters to fit the model to the DNS results (Saito et al. 2021). Equation (12) implements the linear deterministic IEM closure: Two relaxation tendencies act on S'_α, one on τ_L (turbulent mixing) and one on τ_p (condensation/evaporation).

Note that Eq. (12) does not contain a Wiener term to represent the effect of turbulence increasing the variance of S'_α. Oftentimes, such a term represents the influence vertical velocity fluctuations (Grabowski and Abade 2017; Abade et al. 2018; Saito et al. 2021). Here, however, the limited extent of the domain restricts the influence of vertical velocity fluctuations on the supersaturation considerably. And we do not consider this effect in all models analyzed in this study for clarity. As a result, Eq. (12) decays supersaturation fluctuations by contracting the peaks of a bimodal distribution (typical of entrainment interfaces studied here), producing a single unimodal supersaturation distribution.

By combining $\overline{S}$ and S'_α, the growth of droplets is expressed as

$$r_\alpha \frac{dr_\alpha}{dt} = K(\overline{S} + S'_\alpha). \tag{13}$$

Thus, condensational growth is determined by S'_α, i.e., a quantity immanent to a specific Lagrangian fluid element. This constitutes a fundamental difference to the representation of condensational growth in DNS and LEM, in which S is evaluated at a specific location in space.

d. RMM

Next, we apply the one-dimensional statistical model by Fries et al. (2021) based on ideas by Pope (2000). The approach is similar to the IEM presented above but considers a space-dependent mean to which the Lagrangian fluid elements relax, making it necessary also to predict the motion of these fluid elements. Note that we do not show the nondimensional equations of Fries et al. (2021) to ease comparison with the other models presented here.

In the RMM, two types of fluid elements are simulated, those that contain droplets and those that do not. It is assumed that the droplets move with the fluid elements. The displacement of a fluid element along the one-dimensional domain is given by

$$\frac{dx_\alpha}{dt} = u_\alpha, \tag{14}$$

and their motion is described by the Langevin equation

$$du_\alpha = -\frac{u_\alpha}{\frac{4}{3}\tau_L / C_0}dt + (\tau_L \varepsilon C_0)^{1/2} dW. \tag{15}$$

The first term describes the autocorrelation of a fluid element's motion, with $(4/3)\tau_L/C_0$ being the autocorrelation time scale (Fries et al. 2021), and the parameter C_0 according to Pope (2011). The second term represents turbulent motion as Brownian increments, with dW being an increment of a Wiener process with zero mean and variance dt/τ_L (Pope 1991). The $(\tau_L \varepsilon C_0)^{1/2}$ is the standard deviation of the velocity increments. Equation (15) randomizes the kinematics of fluid elements described by Eq. (14); it is not a scalar mixing term.

Similar to Eq. (12) in the IEM, S_α is determined by

$$\frac{dS_\alpha}{dt} = -C_{\mathrm{RMM},1}\frac{S_\alpha - \langle S(x_\alpha, t)\rangle}{\tau_L} - C_{\mathrm{RMM},2}\frac{\langle r(t)S(x_\alpha, t)\rangle / r_i}{\tau_{p,i}} \tag{16}$$

but considers, in the first term, the relaxation of S_α to $\langle S(x_\alpha, t)\rangle$, where $\langle..\rangle$ indicates an ensemble average. This space-dependent

quantity is determined from all simulated fluid elements located around x_α at t using kernel estimates, as detailed in Pope (2000). The half-width of the kernel is slightly less than 1% of the model domain, chosen as a trade-off between statistical noise and averaging bias (Pope 2000). The second term describes the effect of condensation and evaporation and can be derived from Eq. (4). Similar to the first term, $\langle r(t)S(x_\alpha, t)\rangle$ is an ensemble average determined from all simulated fluid elements around x_α at t. Here, r_i and $\tau_{p,i}$ are the initial droplet radius and phase relaxation time scale, respectively. The $C_{\mathrm{RMM},1}$ and $C_{\mathrm{RMM},2}$ are the empirical constants.

Droplet condensational growth is determined as

$$r_\alpha \frac{dr_\alpha}{dt} = KS_\alpha, \tag{17}$$

similar to IEM. However, S_α is linked to x_α, which enables RMM to consider spatial information of the mixing process that is missing in the IEM's implementation used here.

To summarize, the RMM considers spatial dependence by relaxing each fluid element's S_α toward a space-dependent mean $\langle S(x_\alpha, t)\rangle$ [Eq. (16)], and it couples to condensation/evaporation through the conditional mean $\langle r(t)S(x_\alpha, t)\rangle$. However, droplet-laden and droplet-free elements do not exchange composition internally, so RMM does not produce new subgrid supersaturation variability by entrainment mixing itself; it only advects and relaxes toward the resolved-scale mean. Consequently, RMM captures some asymmetry (high S from cloudy interiors) but misses the lowest ambient S and underbroadens the S distribution compared with DNS, LEM, and MCM (cf. Figs. 7 and 8).

e. MCM

Last, we apply another statistical model by Fries et al. (2023), which employs the mapping-closure approach by Chen et al. (1989) and Pope (1991) to better represent supersaturation fluctuations.

Similar to the RMM, the MCM is based on replacing T and q_v with a single equation for S,

$$\frac{\partial S}{\partial t} + \mathbf{u}\cdot\boldsymbol{\nabla}S = D\boldsymbol{\nabla}^2 S + \frac{1}{q_{vs}(T_0, p_0)}C_d, \tag{18}$$

where T_0 and p_0 are the reference temperatures and pressures, respectively. To retrieve S, MCM does not solve Eq. (18) directly but employs a mapping X from a time-independent Gaussian-distributed random variable $\xi(t)$, with zero mean and unit variance, to $S(\mathbf{x}, t)$, which—in a statistical sense—is interpreted as an arbitrarily distributed random variable. Accordingly, for a given $\mathbf{x}$ and t,

$$S(\mathbf{x}, t) = X\{\xi[\mathbf{x}/\lambda_{\mathrm{MCM}}(t)], t\}, \tag{19}$$

where $\lambda_{\mathrm{MCM}}(t)$ is a time-dependent length scale. By inserting Eq. (19) in Eq. (18), with some further considerations detailed in Fries et al. (2023), X is predicted as

$$\frac{\partial X}{\partial t} = \varphi(t)\left(-\delta\frac{\partial X}{\partial \delta} + \frac{\partial^2 X}{\partial \delta^2}\right) - \frac{\tau_L}{\tau_{p,i}}\langle C_d | S = X\rangle, \tag{20}$$

where δ is the sample-space variable corresponding to ξ, with the sample space containing all possible realizations of ξ. Further, $\varphi(t)$ is a relaxation rate and $\langle C_d | S = X\rangle$ is a conditional ensemble-averaged condensation rate. The $\varphi(t)$ and the aforementioned $\lambda_{\mathrm{MCM}}(t)$ are unknown for most applications. Hence, they are determined from DNS here, while theoretical closures may exist for specific cases.

Similar to Eqs. (12) and (16) in IEM and RMM, MCM predicts ξ_α for multiple fluid elements using a Langevin equation, such that

$$d\xi_\alpha = -R(t)\xi_\alpha dt + \sqrt{2R(t)}\, dW. \tag{21}$$

This approach ensures that the ensemble of ξ_α relaxes to a Gaussian as assumed for ξ above. Moreover, Fries et al. (2023) set $R(t) = C_{\mathrm{MCM}}\varphi(t)$, with C_{MCM} being a fitting parameter from DNS.

Similar to IEM and RMM, the droplet condensational growth equation is

$$r_\alpha \frac{dr_\alpha}{dt} = KX(\xi_\alpha, t). \tag{22}$$

Here, however, the mapping X is crucial to determine S from ξ_α via Eq. (19).

Throughout, we use "supersaturation history" to describe the time series $S_\alpha(t)$ experienced by droplets or droplet-bearing Lagrangian elements, whose time integral sets droplet growth by Eqs. (6), (10), (13), (17), and (22). Figures showing time series and time-evolving distributions report statistics of these histories.

3. Case setup

We simulate the mixing of a cloudy filament with dry air. In this section, we will summarize the setup of the simulated cases and how the different models are initialized.

a. Simulated cases

All models simulate a domain that is characterized by the length scale $L_x = 51.2$ cm, irrespective of the dimensionality of the considered approach. All simulations are run for 40 s. Without the aim to simulate a specific cloud type, we prescribe reference values typical for low-level clouds (e.g., shallow cumulus or stratocumulus), with $T_0 = 271$ K, $\rho_0 = 1.06$ kg m^{-3}, and $p_0 = 824.6$ hPa.

To represent the mixing of a cloudy filament with dry air, we initialize q_v and T such that they depict the change from dry to cloudy air along each model's primary dimension, following the original setup proposed by Kumar et al. (2014). We assume that the model's primary dimension is the x axis. Thus,

$$q_{v,i}(x) \equiv q_v(x, t = 0) = (q_{v,c} - q_{v,e})\exp\left[-\lambda\left(x - \frac{L_x}{2}\right)^8\right] + q_{v,e}, \tag{23}$$

TABLE 1. Parameters for the initial T, q_v, and S profiles.

	T_e (K)	$q_{vs,e}$ (g kg^{-1})	$q_{v,e}$ (g kg^{-1})	S_e (—)	T_c (K)	$q_{vs,c}$ (g kg^{-1})	$q_{v,c}$ (g kg^{-1})	S_c (—)
n_0	271.4099	4.048	0.031	−0.9922	270.7535	3.866	4.015	0.038 52
n_1	271.3074	4.019	1.027	−0.7444	270.8151	3.883	4.015	0.034 03
n_2	271.2049	3.990	2.023	−0.4929	270.8768	3.899	4.015	0.029 57
n_3	271.1025	3.962	3.019	−0.2379	270.9384	3.916	4.015	0.025 13

with $q_{v,e}$ being the minimum of q_v found in the environment, $q_{v,c}$ being the maximum of q_v inside the cloud, and $\lambda = 1.45 \times 10^{-10}$ cm^{-8}. The T profile is

$$T_i(x) \equiv T(x, t = 0) = T_0\left\{1 - \left(\frac{R_v}{R_d} - 1\right)[q_{v,i}(x) - q_{v,e}]\right\}, \tag{24}$$

where R_d is the gas constant of dry air. The corresponding initial S_i profile is determined from $q_{v,i}$ and T_i via Eq. (1).

To investigate the impact of ambient humidity, we vary $q_{v,i}$ by adapting $q_{v,e}$ as

$$q_{v,e} = q_{v,e}^{\text{original}} + n\frac{q_{v,c} - q_{v,e}^{\text{original}}}{4}, \tag{25}$$

with n from 0 to 3 and $q_{v,e}^{\text{original}}$ taken from Kumar et al. (2014). The corresponding setups are called from n_0 to n_3, respectively. The resultant values for T, q_v, q_{vs}, and S in the environment (subscript e) and in the cloud (subscript c) are summarized in Table 1. To assess the impact of turbulence, ε is varied between 1 and 1000 cm^2 s^{-3}, with the corresponding turbulence parameters stated in Table 2.

Cloud droplets are initialized as monodisperse particles with initial radii $r_i = 5$ or 15 μm in the central 22 cm of the domain. We refer to this part of the domain as the cloudy part. Note that although the cloudy part covers most of the supersaturated domain, these regions are not identical due to the varying ambient humidity. For all cases, the same domain-averaged $N_{c,i} = 47$ mg^{-1} is initialized, corresponding to 109 mg^{-1} in the cloudy part. This results in $q_{c,i} = 0.06$ g kg^{-1} or 1.54 g kg^{-1} for $r_i = 5$ or 15 μm in the cloud part. Figure 1 summarizes the initial profiles for $q_{v,i}$, T_i, S_i, and $q_{c,i}$ for all thermodynamic setups (n_0–n_3) and r_i.

All models use the parameters summarized in Table 3. Moreover, to ease comparability, all models use the same:

$$q_{vs}(T, p) = \frac{R_d}{R_v}\frac{e_s(T)}{p - e_s(T)} \approx \frac{R_d}{R_v}\frac{e_s(T)}{p}, \tag{26}$$

with

$$e_s(T) = b_{s,1}\exp\left(-\frac{b_{s,2}}{T}\right), \tag{27}$$

TABLE 2. Turbulence parameters used in this study.

ε (cm^2 s^{-3})	1	10	33.75	100	1000
TKE (cm^2 s^{-2})	7	34.4	78.8	168.1	799.9
τ_L (s)	7	3.44	2.34	1.68	0.8

and the parameters $b_{s,1} = 2.53 \times 10^8$ kPa and $b_{s,2} = 5420$ K from Rogers and Yau (1989).

b. Model initialization

In DNS and LEM, the initial distributions of $q_{v,i}$, T_i, and, hence, S_i are represented on a numerical grid with resolutions of 1.0 and 0.1 mm and 134 217 728 and 5120 grid boxes, respectively. In the initially cloudy part of the domain, the approaches initialize 6 771 519 and 2594 Lagrangian cloud droplets at random $\mathbf{x}_{\alpha,i}$ and $x_{\alpha,i}$, respectively. For DNS and LEM, $r_{\alpha,i} = r_i$ for all simulated droplets initially.

For IEM, $\overline{S_i}$ is determined from $\overline{T_i}$ and $\overline{q_{v,i}}$. The $S'_{\alpha,i}$ is calculated such that $\overline{S_i} + S'_{\alpha,i} = S_i(x_i)$, where x_i are the randomly picked locations in the cloudy region. (Note that x_i is only relevant during the initialization and is not considered in subsequent calculations of the IEM.) In total, 2594 Lagrangian cloud droplets are simulated, with their initial $r_{\alpha,i} = r_i$.

RMM assigns $S_{\alpha,i} = S_i(x_{\alpha,i})$ to Lagrangian fluid elements at random locations $x_{\alpha,i}$. The fluid elements are of two types, representing air with or without droplets, respectively. The 1.4×10^5 air elements are initialized in the entire domain, and 2×10^5 droplet elements are initialized within the cloudy part. The latter are assigned the radius $r_{\alpha,i} = r_i$, while the prior $r_{\alpha,i} = 0$ throughout the simulation.

MCM determines the initial mapping X_i from the relation $F_i[X_i(\delta)] = \Gamma(\delta)$, where $F_i(S)$ is the initial cumulative distribution function (CDF) of S from DNS and $\Gamma(\dots)$ is the CDF of a standardized Gaussian-distributed variable. One proceeds by sampling 10^6 fluid elements with $\xi_{\alpha,i}$ from a standardized Gaussian conditional on that they are mapped to a supersaturation $X_i(\xi_{\alpha,i})$ found within the droplet-containing region of the initially cloud part of the domain. The fluid elements are assigned the initial radius $r_{\alpha,i} = r_i$.

Simulations using the LEM and IEM are repeated each 1000 times to gain reliable ensemble averages. Because RMM and MCM compute a much larger number of fluid elements, ensemble-averaging is not necessary. Also for DNS, results from only one simulation are considered.

4. Results

a. General development

The qualitative behavior of the mixing process is demonstrated in Fig. 2, showing LEM results for $r_i = 5$ μm, n_0 thermodynamics, and $\varepsilon = 1$ cm^2 s^{-3}. The initially supersaturated cloudy part (Fig. 2a) is depleted by cloud droplet condensation, resulting in a momentary increase in q_c and the average cloud droplet radius r_m (Figs. 2b,d). Note that our analysis

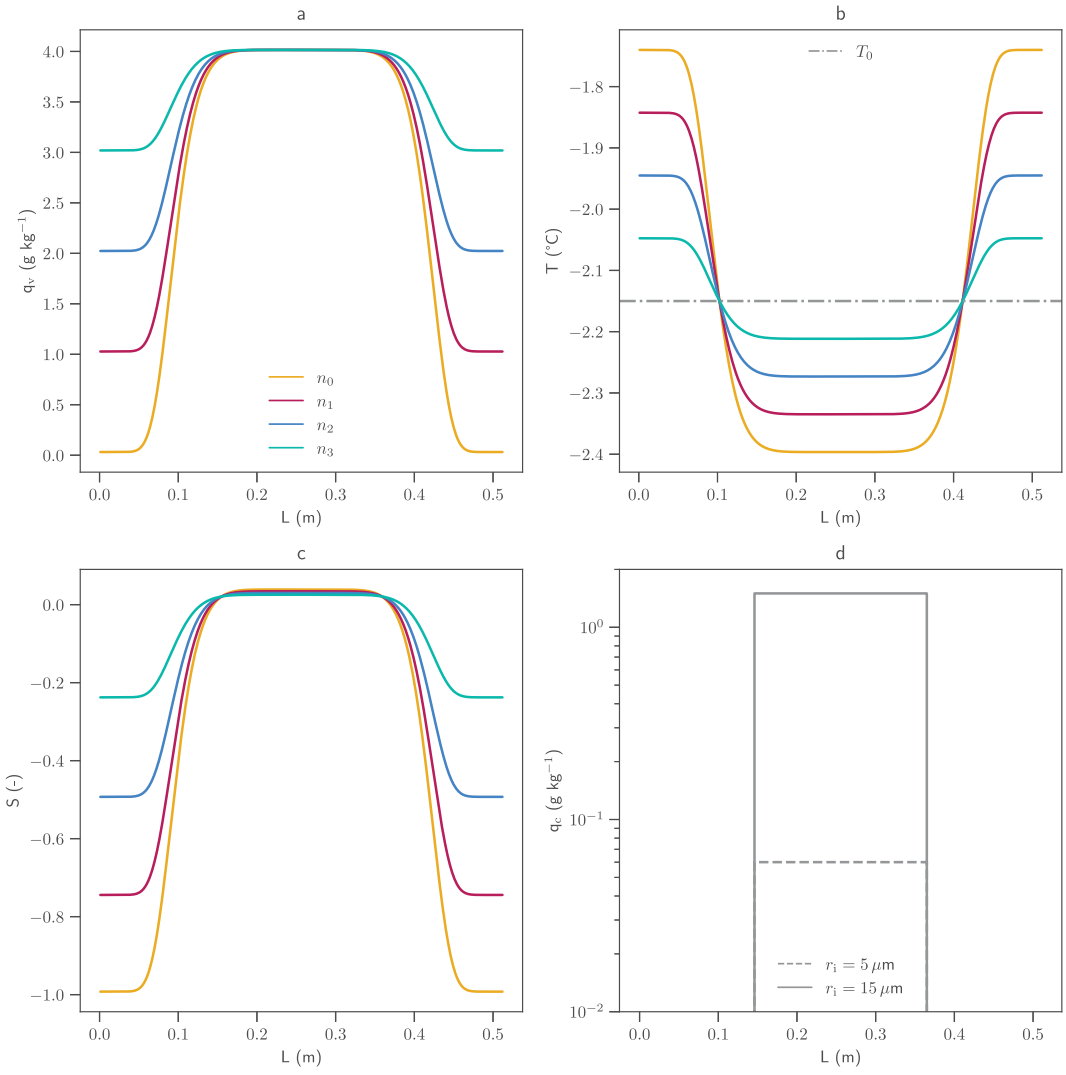

FIG. 1. Initial (a) $q_{v,i}$, (b) T_i, (c) S_i, and (d) $q_{c,i}$ profiles for different thermodynamics (denoted n_0–n_3, colored lines) or r_i (gray lines). In (b), the reference temperature T_0 is shown (gray dashed–dotted line).

defines cloud droplets as any particle with $r > 0.5$ μm. At the same time, however, the cloud is mixed with its subsaturated surroundings, which decreases S and N_c constantly (Figs. 2a,c). After about 3 s, net condensation switches to evaporation (Fig. 2b), and all droplets evaporate until the end of the simulation, at which a fully subsaturated domain establishes (Figs. 2a,b). Note that for more humid thermodynamic cases (n_1–n_3), the domain saturates toward the end of the simulation, which prevents the full evaporation of all droplets (not shown).

TABLE 3. Further parameters used in this study.

Quantity	Symbol	Unit	Value
Kinematic viscosity	ν	m^2 s^{-1}	1.5×10^{-5}
Molecular diffusivity of heat	D_κ	m^2 s^{-1}	2.23×10^{-5}
Molecular diffusivity of water vapor	D_v	m^2 s^{-1}	2.16×10^{-5}
Enthalpy of vaporization	l_v	J kg^{-1}	2.5×10^6
Specific heat of air at constant pressure	c_p	J K^{-1} kg^{-1}	1005.0
Density of liquid water	ρ_l	kg m^{-3}	1000.0
Gas constant of water vapor	R_v	J K^{-1} kg^{-1}	461.5
Gas constant of dry air	R_d	J K^{-1} kg^{-1}	287.0
Thermal conductivity	κ	J m^{-1} s^{-1} K^{-1}	2.38×10^{-2}

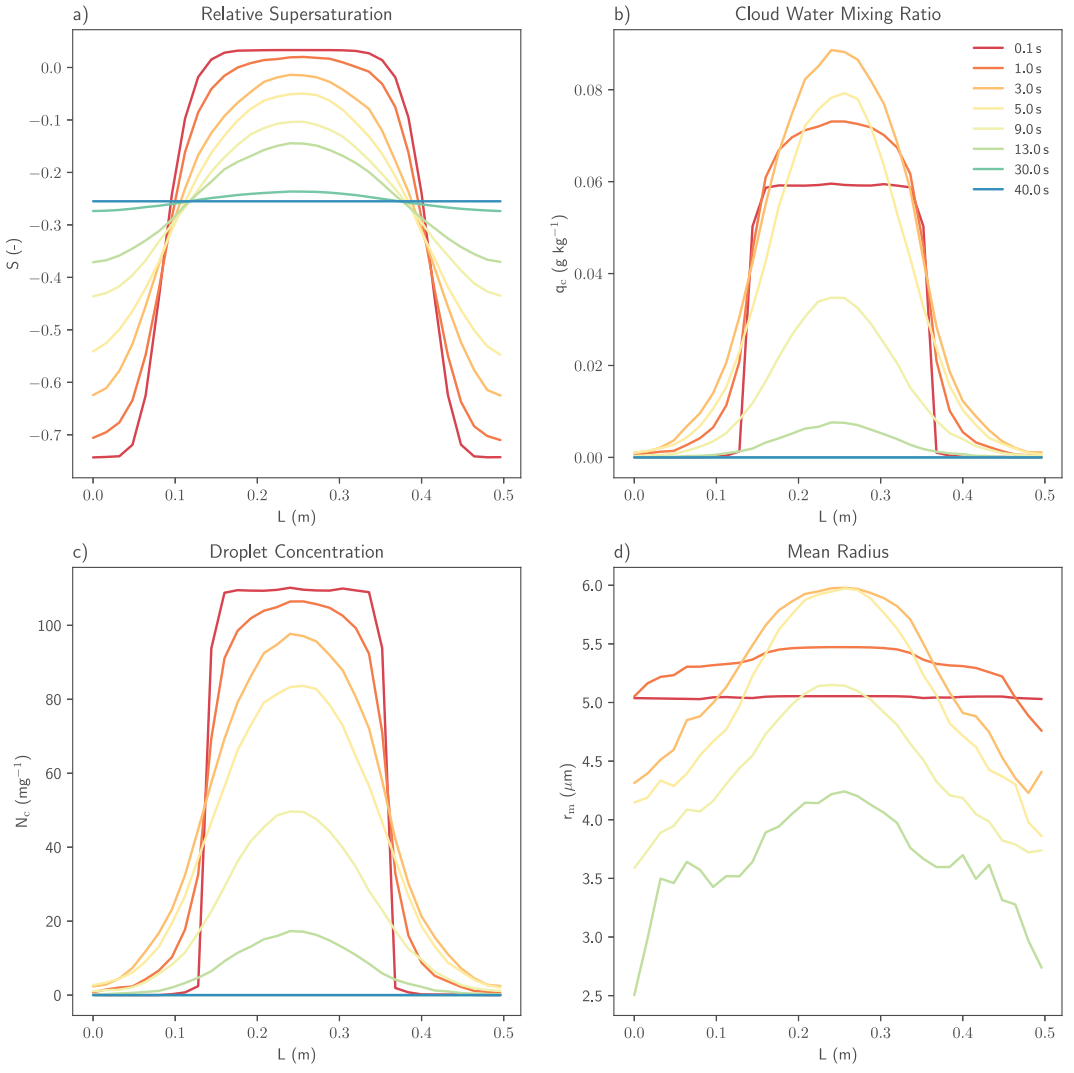

FIG. 2. For individual time steps (from red to blue), the development of (a) the relative supersaturation, (b) q_c, (c) the droplet concentration, and (d) the conditional average of the droplet radius are shown along the entrainment profile. The r_m is calculated as an arithmetic mean of an ensemble of 1000 simulation runs, where only grid boxes that contain at least one particle are taken into account.

b. *Sensitivity on turbulence intensity*

Now, we assess how changes in the degree of turbulence are captured by the models. Figures 3a–d show the temporal evolution of the domain-averaged q_v, T, q_c, and S for different ε but the same $r_i = 5$ μm and n_1 thermodynamics. For readability, we omit $\overline{(..)}$ to indicate domain averages in the following. Moreover, line colors indicate ε, and line patterns indicate the analyzed models. Irrespective of ε, DNS data are shown by a thin black line to ease their identification.

As discussed for Fig. 2, the initially supersaturated cloudy part causes condensation during the onset of the simulation, resulting in a momentary reduction in q_v (Fig. 3a), a release of latent heat (Fig. 3b), an increase in q_c (Fig. 3c), and a decrease in S (Fig. 3d). The initial condensation is followed by the complete evaporation of all droplets and a domain void of q_c at the end of the simulation (Fig. 3c). As for the initial condensation phase, the time scale for this process is determined by ε, which determines how quickly the cloud mixes with the ambient air. Specifically, the strongest $\varepsilon = 1000$ cm^2 s^{-3} leads to complete evaporation within 3 s, while the smallest $\varepsilon = 1$ cm^2 s^{-3} allows the cloud to survive for 20 s.

Overall, the above-described behavior is captured by all models, with minor differences in the mixing rate. These are probably due to slight disagreements in the representation of a specific turbulence intensity but much smaller than those caused by the analyzed variations in ε. Moreover, we see a distinct offset in S predicted by RMM and MCM (Fig. 3d). Because DNS did not provide a domain-averaged S, S is determined from the domain-averaged q_v and T for DNS, LEM, and IEM. On the other hand, RMM and MCM do not predict q_v and T but S directly. Thus, the offset is a result of the

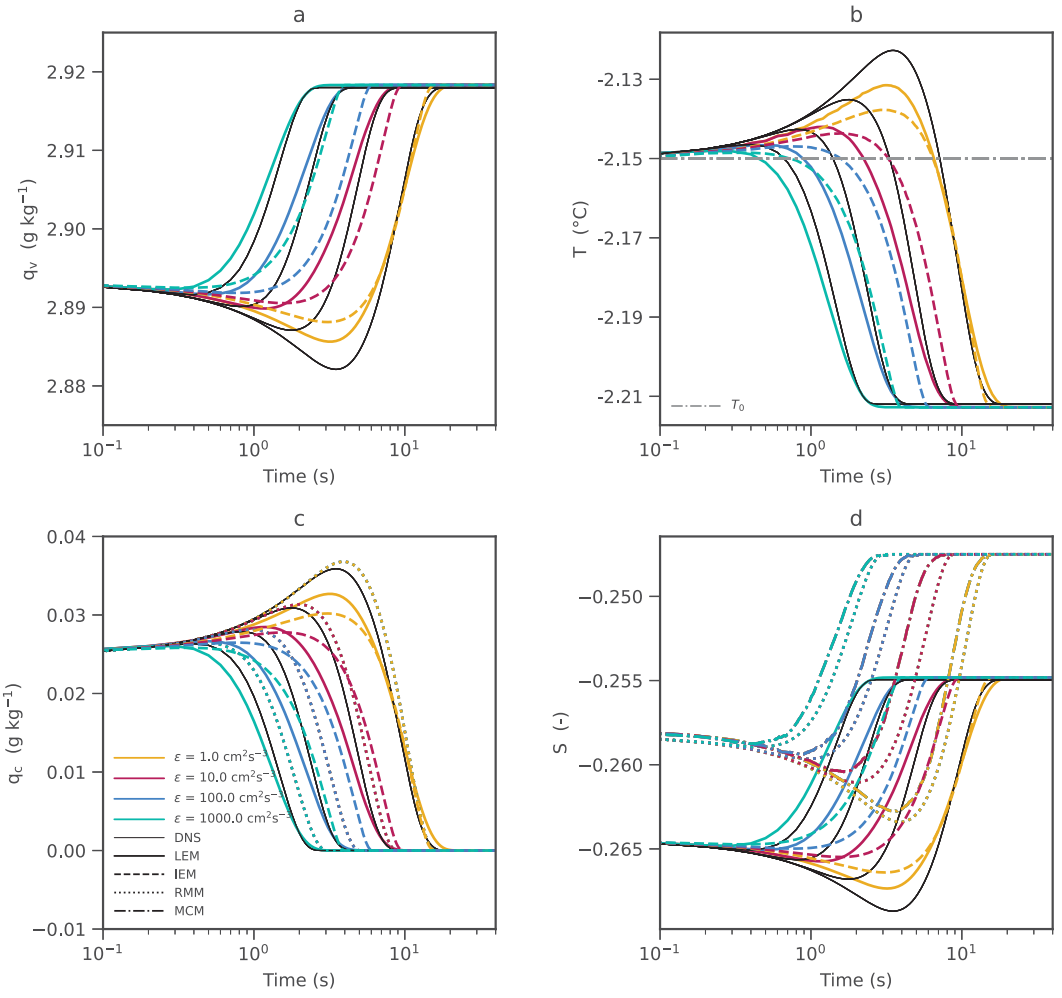

FIG. 3. Time evolution of the domain-averaged, that is, arithmetic mean of all grid boxes (a) q_v, (b) T, (c) q_c, and (d) S for four different energy dissipation rates (colors) and five models (pattern). Note that the DNS results are always in black to highlight them.

nonlinear dependency of S on T that is not appropriately considered when a domain-averaged T is used to determine the domain-averaged S. However, this discrepancy has no impact on the simulated physics, as the time series for q_c suggests (Fig. 3c).

The slow initial rise of supersaturation in the IEM, which is visible as the muted slopes of dS/dt, in Figs. 3d and 4d, stems, among other factors, from the way Eq. (12) has been simplified for the present study. By removing the Wiener process term used by Grabowski and Abade (2017) and Abade et al. (2018), IEM now contains only two deterministic relaxation tendencies: one that erodes the supersaturation fluctuation S'_α on τ_L (mixing) and one that damps it much more quickly with τ_p (condensation/evaporation). Because no stochastic vertical velocity forcing remains to counter those sinks, S' caused by the model's initialization decays fast. In other words, the model behaves as an overdamped Ornstein–Uhlenbeck process which mean quickly approaches a steady, near-zero value. Consequently, N_c stays nearly constant until r_m has already shrunk appreciably, resulting in the comparatively homogeneous signature seen later in Figs. 4a–c. Adding a stochastic supersaturation forcing or reducing τ_p would accelerate the early growth of S and its derivative, but here we retain the deterministic form to keep the model structure consistent across all statistical approaches examined. In fact, retaining only the deterministic relaxation terms in Eq. (12) is warranted for our configuration because the stochastic vertical velocity forcing becomes insignificant once the integral length scale collapses to the present $L_{\text{outer}} = 0.512$ m at which the associated noise amplitude $\sigma_{w'} \propto \sqrt{\varepsilon \tau_L C_0}$ never exceeds 0.02 m s^{-1} even at $\varepsilon = 1000$ cm^2 s^{-3} and is, therefore, an order of magnitude smaller than the deterministic mixing tendency. Any residual influence of such small fluctuations is absorbed by tuning the two relaxation coefficients $C_{\text{IEM},1}$ and $C_{\text{IEM},2}$ to the DNS reference, eliminating the need for an additional parameter while still reproducing the bulk statistics shown in Figs. 3 and 4.

Figures 4a and 4b show the domain-averaged N_c and r_m, respectively, while Fig. 4c juxtaposes these quantities to illustrate

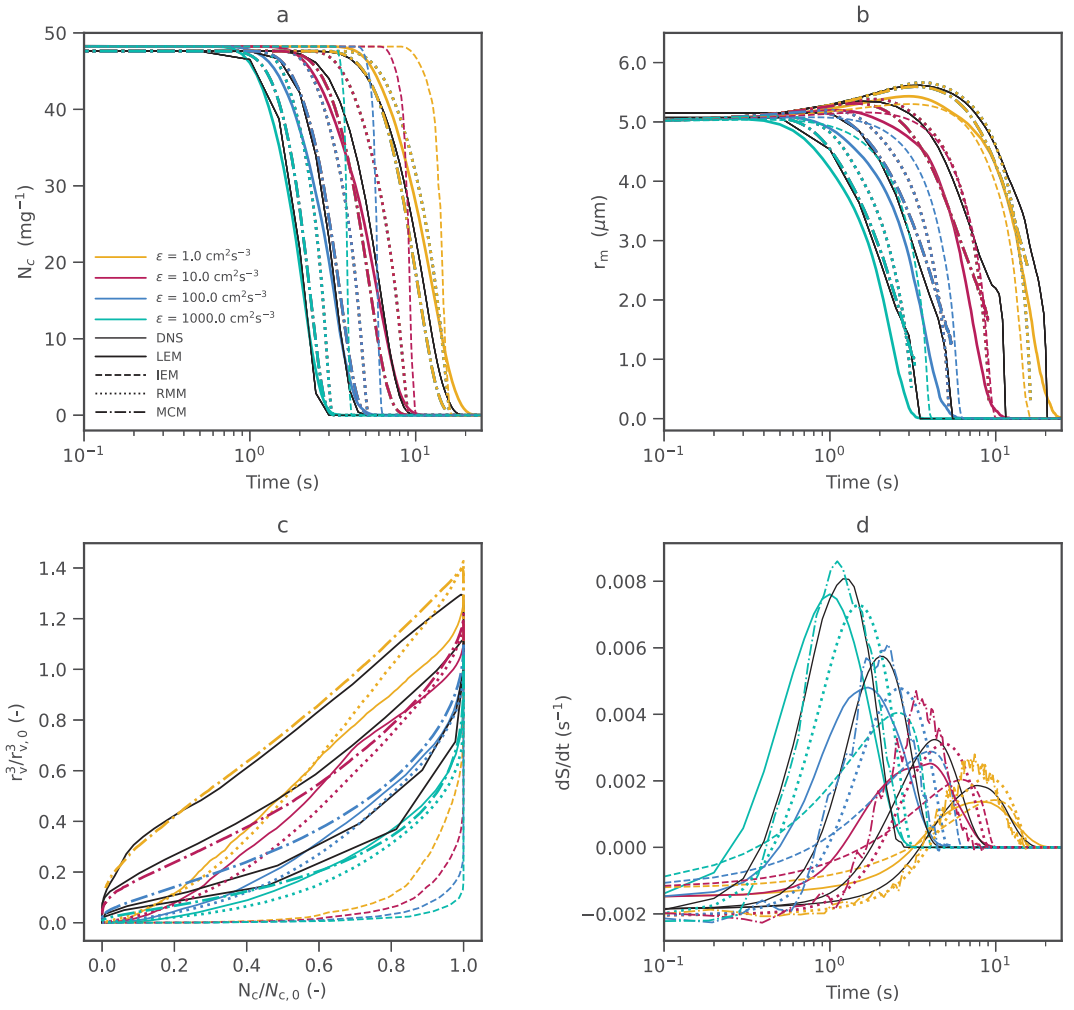

FIG. 4. Time evolution of the domain-averaged, that is, arithmetic mean of all grid boxes (a) N_c, (b) r_m, (c) the mixing diagram, and (d) the change rate of S for four different energy dissipation rates (colors) and five models (pattern). Note that the DNS results are always in black to highlight them.

their covariability, as similarly done in microphysical mixing diagrams (e.g., Burnet and Brenguier 2007). While r_m increases during the initial condensation phase, N_c remains at its initial value. In the evaporation phase, all models show a decrease in r_m, with full evaporation toward the end of the simulation. Interestingly, DNS, LEM, RMM, and MCM show a gradual decrease in N_c, while IEM predicts a constant N_c until r_m reaches 0. This behavior indicates that DNS, LEM, RMM, and MCM can represent inhomogeneous mixing, which is characterized by a decrease in N_c due to the full evaporation of some droplets during the mixing process. IEM, however, seems to be biased toward homogeneous mixing, during which all droplets evaporate simultaneously, but none fully, resulting in a constant N_c as long as not all droplets evaporate completely.

c. *Sensitivity on ambient humidity*

Next, we test the susceptibility of all models to different ambient humidities, represented by the thermodynamic cases n_0–n_3, all with $r_i = 15$ μm and $\varepsilon = 33.75$ cm^2 s^{-3}. Particularly, we investigate cases in which the cloud does not fully evaporate by the end of the simulation (cases n_1–n_3). As above, Fig. 5 displays the temporal evolution of the domain-averaged q_v, T, q_c, and S. Again, all models capture the behavior well. Note, however, that differences among the models are less visible than for section 4b due to the larger range of values covered in the respective ordinates. Particularly, the above-discussed offset in S from RMM and MCM is still present, as well as the same minor variability in the mixing rate. By the end of the mixing process, however, all models agree. This is not surprising since the end state is solely determined by thermodynamics, i.e., all models should reach the same state irrespective of cloud microphysics and dynamics. For RMM and MCM, however, this is only possible since the variability in T is sufficiently small (Fig. 5b) to not violate the underlying assumption of a constant T_0 to determine S.

In Figs. 6a and 6b, the domain-averaged N_c and r_m are shown. Figure 6c shows the corresponding mixing diagram.

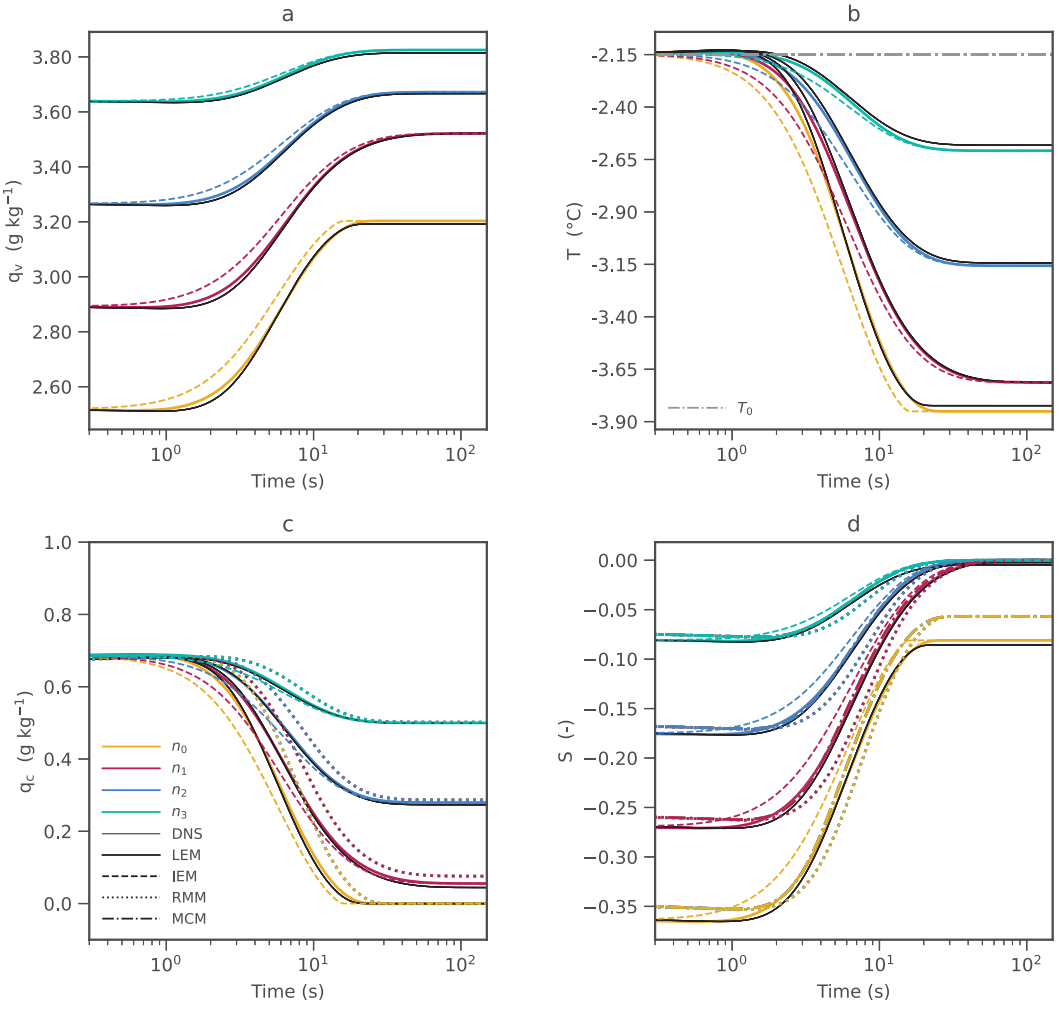

FIG. 5. Time evolution of the domain-averaged (a) q_v, (b) T, (c) q_c, and (d) S for four different ambient humidities (colors) and five models (patterns). Note that the DNS results are always in black to highlight them. In (b), the reference temperature T_0 is shown (gray dashed–dotted line).

While most models show again a very good agreement with the DNS, we still see that the IEM is not capable of capturing the gradual decrease in N_c but rather represents an abrupt drop when all droplets evaporate. This effect is especially apparent not only for n_0 (orange lines) where the strongest evaporation takes place but also for n_1 (red lines). As before, this indicates a bias toward homogeneous mixing in the IEM, while all other models indicate more inhomogeneous mixing.

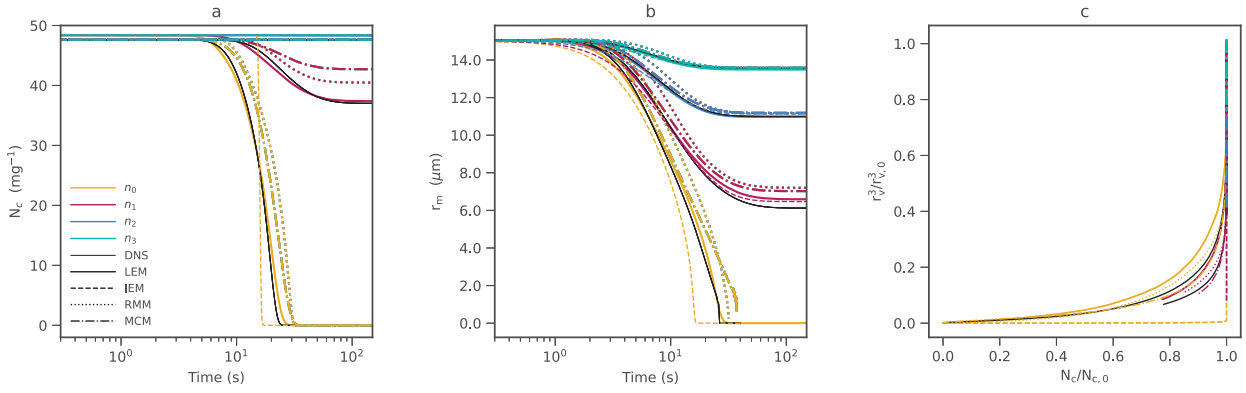

FIG. 6. Time evolution of the domain-averaged (a) N_c, (b) r_m, and (c) the mixing diagram for four different ambient humidities (colors) and five models (patterns). Note that the DNS results are always in black to highlight them.

d. Supersaturation spectra and droplet size distributions

The ability of the presented models to represent the mixing process breaks down to their ability to accurately capture the development of S and, hence, each droplets' growth history. For $\varepsilon = 1$ and 1000 cm^2 s^{-3}, the thermodynamics n_1, and $r_i = 5$ μm, Lagrangian supersaturation spectra and the corresponding droplet size distributions are presented in Figs. 7 and 8. Here, the term Lagrangian supersaturation refers to the supersaturations experienced by droplets.

During the onset of the mixing process (1 s), DNS and LEM show an asymmetric S distribution, consisting of high S from the cloud and lower ambient S experienced by those droplets already mixed outside of the cloud (Figs. 7a,c and 8a,c). In particular, within the first second of the simulations with $\varepsilon = 1$ cm^2 s^{-3}, we observe qualitative differences in the models (Fig. 7). The LEM model in particular produces a tail toward lower droplet radii, due to the way it initiates mixing. In the LEM, an individual grid box may be reshuffled to a region of the domain where the lower end of the supersaturation spectrum can be found. If this occurs, molecular diffusion reduces S to a level that forces the immediate and rapid evaporation of droplets. This results in a broader spectrum of droplet radii in the LEM domain compared to the other models, which either more accurately represent turbulent mixing (DNS) or follow a stochastic relaxation procedure (MCM, RMM, IEM). The contrasting S distribution evolutions are consistent with the closures: DNS and LEM create intermittent filaments and entrainment interfaces that broaden and skew the distribution, MCM inherits this via a mapping closure that evolves the full distribution, IEM contracts the distribution without shape relaxation, and RMM partially offsets this by relaxing to a space-dependent mean. Broad, often negatively skewed supersaturation distributions are expected from isobaric mixing and entrainment (e.g., Gaussian-mixing models and LES show negative skewness), whereas IEM-type closures cannot create this skewness on their own (e.g., Thomas et al. 2021). As expected, the mode of the S distribution shifts to lower values as the mixing evolves. At the same time, the S distribution also narrows, indicating the homogenization of cloudy and ambient air, resulting in a more Gaussian distribution of S. This behavior is especially visible for $\varepsilon = 1000$ cm^2 s^{-3} where mixing is stronger (Fig. 8), while the case with $\varepsilon = 1$ cm^2 s^{-3} maintains a broader and more asymmetric distribution throughout the mixing process (Fig. 7). As the MCM relaxes to a Gaussian S distribution by design, it fails to represent the later S distributions for $\varepsilon = 1$ cm^2 s^{-3} (Fig. 7e), while it agrees well with the DNS for $\varepsilon = 1000$ cm^2 s^{-3} (Fig. 8e). RMM and IEM largely fail to represent the broadening of the S distribution (Figs. 7g,i and 8g,i). While IEM assumes a very narrow S distribution that slightly shifts to smaller values, RMM is at least able to represent some asymmetry in the S distribution by including high S from inside the cloud, but it misses representing the lowest ambient S found in DNS.

DNS, LEM, and MCM also agree well in their representation of the droplet size distribution, which contains large droplets from inside the cloud and smaller droplets that have experienced some mixing and evaporation (Figs. 7b,d,f and 8b,d,f). Thus, these models are able to represent inhomogeneous mixing during which some droplets evaporate, while others remain (almost) unblemished. The foundation for this is the ability of these models to represent a broad S distribution (Figs. 7a,c,e and 8a,c,e), as also recently shown by Lim and Hoffmann (2024). The RMM is able to capture this development of the droplet size distribution partially, although the largest droplets evaporate too fast (Figs. 7h and 8h). The IEM shows again a more homogeneous response, where the entire droplet size distribution evaporates to smaller sizes (Figs. 7j and 8j). Note that these differences among the models are especially strong for $\varepsilon = 1$ cm^2 s^{-3} (Fig. 7), which favor inhomogeneous mixing due to the low turbulence intensity, while the differences are smaller for $\varepsilon = 1000$ cm^2 s^{-3} (Fig. 8), which mixes more homogeneously. The inability of IEM and to a lesser extent RMM to recover the DNS, LEM, and MCM behavior in S (including the low-S tail from entrained ambient air) is consistent with IEM's deterministic nature: It cannot relax a two-peaked S distribution toward a unimodal state without an explicit stochastic small-scale mixing mechanism (Duplat and Villermaux 2008; Villermaux and Duplat 2003). By contrast, the MCM does evolve distribution shape and, therefore, reproduces the broad, skewed S distributions and the bimodal-to-unimodal transition commonly associated with turbulent mixing.

5. Discussion

Extending our previous analysis, we now discuss some aspects of the individual models that need to be considered for their (potential) utilization as a subgrid-scale scheme for LES models.

a. Estimating the subgrid-scale variability of S

When applied as a subgrid-scale scheme in LES, the previously discussed approaches will most likely be executed along the cloud microphysical parameterizations used to determine the evolution of cloud droplets in every LES grid box at every LES time step (Hoffmann et al. 2019; Chandrakar et al. 2021). To do so, the LES-unresolved distribution of S (or equivalently q_v and T) must be estimated to initialize the subgrid-scale schemes at every time step.

The IEM implementation presented here is appealing because it relies solely on the gridbox-averaged S predicted by the LES, requiring no further assumptions (Chandrakar et al. 2021). However, our study showed that some information on the subgrid-scale distribution of S can substantially improve the representation of the turbulent mixing process and the cloud microphysical response. For the application of the LEM as an LES subgrid-scale model, Hoffmann et al. (2019) presented a method to diagnose the subgrid-scale variability of S from the history of Lagrangian fluid elements moving through the LES. If this method is also possible for the RMM or the MCM remains to be tested. Additionally, the MCM requires input from DNSs or other sources to consider the (LES unresolved) spatial variability in S. Here, machine learning could help generate closures that depend on the different

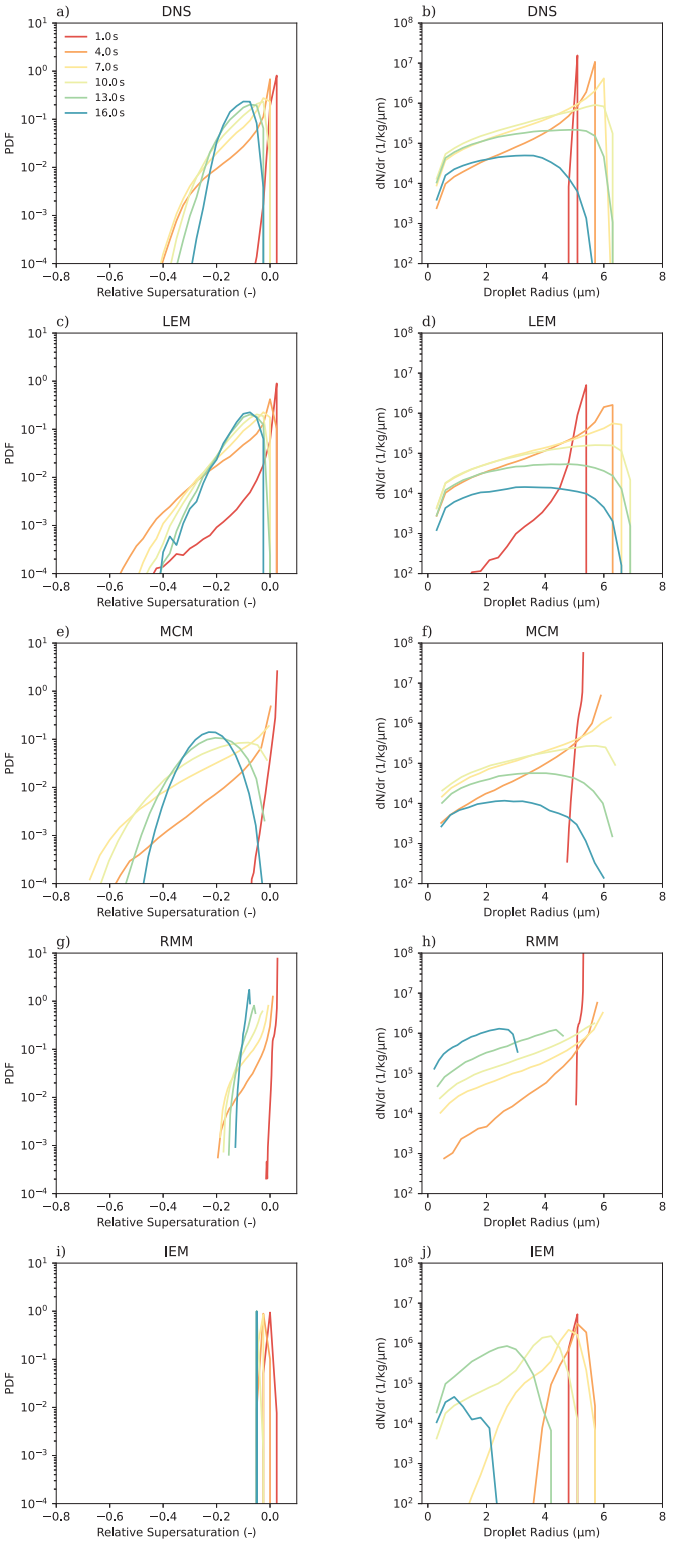

FIG. 7. Time evolution of the (left) supersaturation spectra at the droplets positions and (right) droplet size distributions with n_1 thermodynamics, $r_i = 5$ μm, and $\varepsilon = 1$ cm^2 s^{-3}. Different colors represent individual time steps during the mixing process.

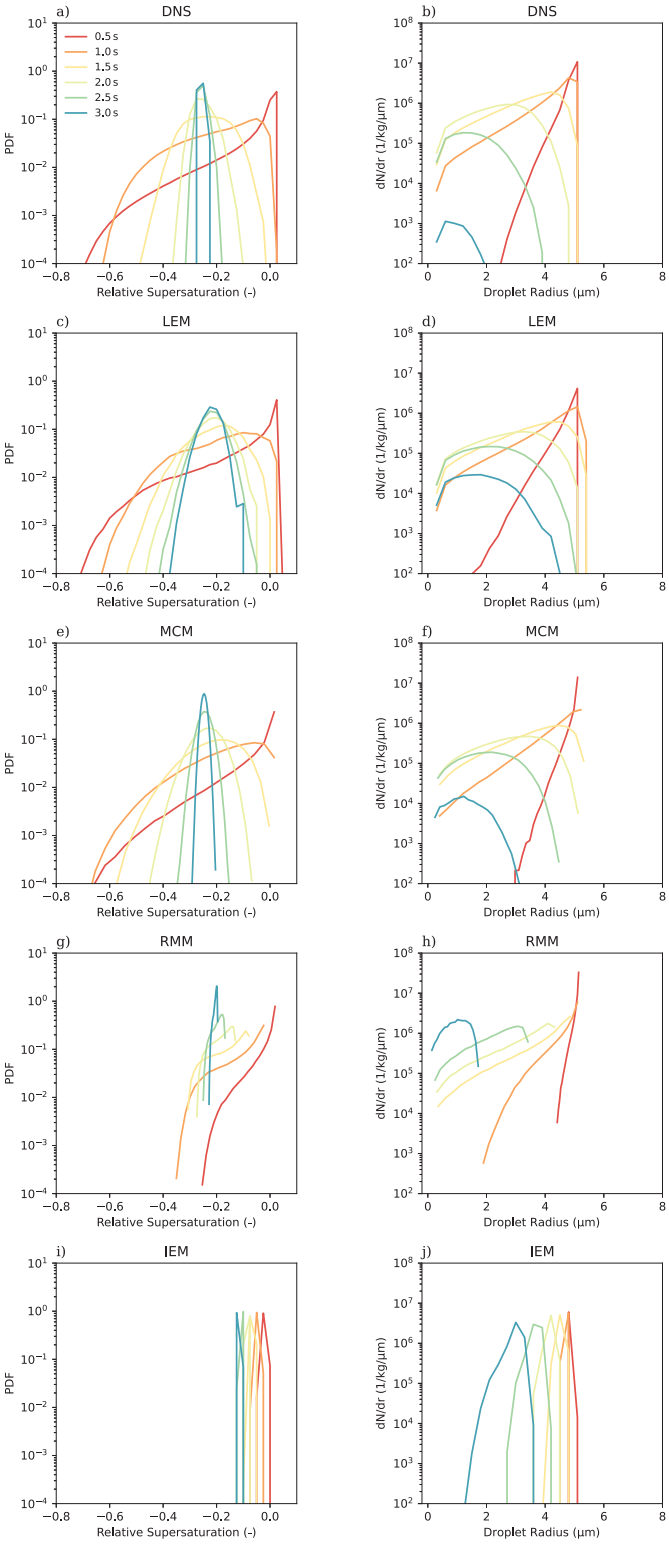

FIG. 8. Time evolution of the (left) supersaturation spectra at the droplets positions and (right) droplet size distributions with n_1 thermodynamics, $r_i = 5$ μm, and $\varepsilon = 1000$ cm^2 s^{-3}. Different colors represent individual time steps during the mixing process.

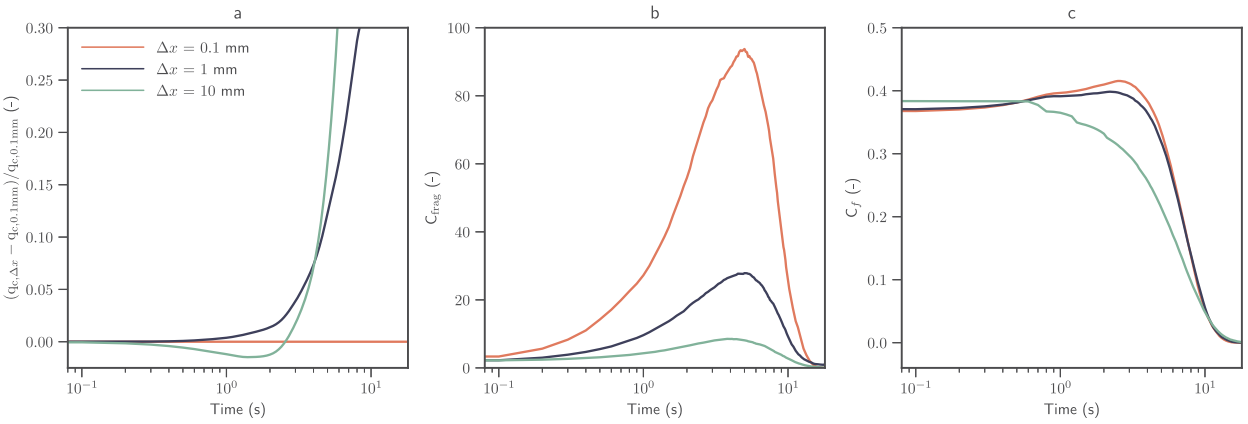

FIG. 9. Time series of (a) the relative q_c difference, (b) the fragmentation of the cloud C_{frag}, and (c) the cloud fraction C_f for different LEM resolutions (line colors).

environments encountered in an LES (e.g., Frezat et al. 2022; Jakhar et al. 2024).

b "A posteriori" nature of the IEM

To represent the thermodynamic development correctly, the IEM needs to be tuned by adjusting the parameters $C_{\text{IEM},1}$ and $C_{\text{IEM},2}$ that steer the impact of mixing and cloud microphysics, as also noted by Saito et al. (2021). For this study, we determined $C_{\text{IEM},1} = 0.18$ and $C_{\text{IEM},2} = 0.03$ as useful tuning parameters for all assessed cases. However, different sets of tuning parameters might be necessary for more different environments that are encountered when the IEM is used as a subgrid-scale model in LES. Interactively adjusting $C_{\text{IEM},1}$ and $C_{\text{IEM},2}$ for a given environment is a challenge that needs to be addressed to further improve the applicability of the IEM as a subgrid-scale model. Put differently, the IEM is a relaxer of a given variability toward the mean. Any "new" variance production by turbulent stirring requires either an explicit stochastic small-scale mixing term in the scalar stochastic differential equation (SDE) or a closure that evolves the full scalar distribution (as done in the MCM), neither of which is part of IEM.

c. LEM's resolution dependency

To represent turbulence down to η, the LEM resolution is required to be smaller than $\eta/6$ (e.g., Menon and Kerstein 2011). Although the LEM requires substantially less computational resources than DNS, the high resolution required by the aforementioned constrain can make LEM relatively costly to operate. Thus, it is customary to apply the LEM at lower resolutions, for which D_κ and D_v are increased appropriately (e.g., Krueger et al. 1997). However, a lower resolution limits the ability of the LEM to represent the details of small-scale mixing.

Figure 9 addresses some impacts when a lower LEM resolution is chosen for $\varepsilon = 1$ cm^2 s^{-3}, $r_i = 5$ μm, and n_1 thermodynamics. The simulations are run with LEM grid spacings $\Delta x =$ 0.1, 1.0, and 10 mm. Figure 9a shows the relative q_c difference from the highest resolution run, i.e., $(q_{c,\Delta x} - q_{c,0.1\text{mm}})/q_{c,0.1\text{mm}}$, with the additional subscript indicating the resolution. One sees clearly that a larger grid spacing first decelerates initial condensation, resulting in a lower q_c, and then slows down the subsequent evaporation of the cloud, maintaining a higher q_c (cf. Fig. 3c). The deceleration of initial condensation can be attributed to the faster decrease in cloud fraction C_f at coarser resolutions, shown in Fig. 9c and determined from the fraction of grid boxes with $q_c > 10^{-2}$ g kg^{-1}. Here, the larger grid spacing combined with the upscaled D_κ and D_v enables ambient air to be transported deeper into the cloud, where it decelerates the initial condensation. At the same time, the higher D_κ and D_v artificially moisten the ambient air. This slows down the subsequent evaporation at coarser resolutions. This interpretation is supported by the higher cloud fragmentation C_{frag} at higher resolutions, shown in Fig. 9b and determined from the number of patches with continuously cloudy grid boxes. (To avoid overestimating C_{frag} at high resolutions, the LEM data are coarse grained using the average distance between two cloud droplets inside the cloud part, about 2 mm.) While C_{frag} remains small during the initial condensation, it quickly increases during evaporation at higher resolutions, indicating a highly intermittent cloud with cloudy patches exposed to (almost unprocessed) ambient air, leading to faster evaporation of some droplets at higher resolution. This analysis indicates that the ability of the LEM to represent inhomogeneous mixing depends on the resolution.

d. Limitations of the single-S approximation

MCM, IEM, and RMM predict S rather than $S(T, q_v)$. This is a common and efficient simplification, but it omits explicit control over the $T - q_v$ cross covariance that shapes S variance (e.g., Chandrakar et al. 2020). In particular, any S variability arising from the nonlinear dependence of $q_{vs}(T)$ on T and q_v is only represented implicitly through the initial conditions and microphysical sinks, not via an explicit covariance closure (Kulmala et al. 1997). While this seems acceptable in our idealized setup, as indicated by the overall good agreement of MCM and DNS, it may become a limitation in flows with persistent inhomogeneities.

6. Summary and conclusions

In this study, we assessed the ability of four statistical turbulence models (the LEM, IEM, RMM, and MCM) to represent the small-scale mixing of cloudy and cloud-free air by comparison with DNS data.

The DNS is treated as ground truth, as it directly solves the underlying Navier–Stokes equations (Kumar et al. 2014, 2017). The LEM employs a mapping approach to mimic how turbulence stretches and folds scalars, i.e., the thermodynamic quantities that drive the condensation and evaporation of cloud droplets during the mixing process (Kerstein 1988; Krueger 1993). The IEM uses a spatially homogeneous process to determine the development of thermodynamics (Pope 1994; Grabowski and Abade 2017), while RMM is able to consider some spatial variability of thermodynamic quantities during the mixing process (Pope 2000; Fries et al. 2021). The MCM uses a mapping closure to predict the non-Gaussian development of thermodynamics during mixing from Gaussian statistics (Chen et al. 1989; Pope 1991; Fries et al. 2023). All models use a similar Lagrangian representation of cloud microphysics.

All statistical turbulence models accurately capture the development of thermodynamics during the mixing process. However, there are differences in the cloud microphysical properties. The differences are traced down to the ability of the statistical turbulence models to represent the supersaturation history experienced by the cloud droplets. We showed that this history is closely linked to the spatial variability of the supersaturation during the mixing process, which contains subsaturations from ambient air as well as supersaturations from the cloud. Only if this broad distribution of supersaturations and its development is represented in a model, it is able to represent inhomogeneous mixing during which some droplets evaporate completely, while others are largely unaffected (Baker and Latham 1979; Lim and Hoffmann 2024). This is the case for LEM, MCM, and partially RMM. The IEM, however, fails to represent this aspect of the mixing process, as all droplets experience approximately the same subsaturation. The resultant constant droplet number concentration can be interpreted as homogeneous mixing.

We have demonstrated that simpler and more computationally efficient models can also capture certain aspects of small-scale cloud-edge mixing. Nevertheless, DNS remains essential for accurately resolving the intricate physical processes that are beyond the scope of these models. However, the applicability of LEM, IEM, RMM, and MCM as subgrid-scale models in LES needs to be evaluated further. LEM and IEM are already used as subgrid-scale models to represent the effects of turbulent supersaturation fluctuations on droplet growth in LESs (Hoffmann and Feingold 2019; Chandrakar et al. 2021). However, for the use of the MCM or RMM as subgrid-scale models, some problems need to be solved (e.g., the generation of highly scenario-specific closure data). Nonetheless, the statistical turbulence models analyzed here constitute practicable means to bridge the gap between small-scale turbulence and clouds and thus constitute a path forward to assess the role of clouds in the climate system in a more holistic framework.

Acknowledgments. J. Kainz and F. Hoffmann were supported by the Emmy Noether program of the German Research Foundation (DFG) under Grant HO 6588/1-1. G. Sardina acknowledges support from Vetenskapsrådet (VR) under Grant 2022-03939, and his computations were enabled by resources provided by the National Academic Infrastructure for Supercomputing in Sweden (NAISS), partially funded by the Swedish Research Council through Grant Agreement 2022-06725. B. Mehlig was supported by VR Grant 2021-4452. The DNS work by B. Kumar, N. N. Makwana, and S. Ravichandran has been carried out using High-Performance Computing System (HPCS) facility available at IITM. The IITM is fully funded by the Ministry of Earth Sciences, Government of India. S. R. is also supported through the Monsoon Mission project IITM/MM-III/2023/IND-4. The authors want to thank Grigory Sarnitsky for useful discussions that improved the quality of the study.

Data availability statement. All data produced for this study are publicly available via the Zenodo repository (Kainz et al. 2024).

REFERENCES

Abade, G. C., W. W. Grabowski, and H. Pawlowska, 2018: Broadening of cloud droplet spectra through eddy hopping: Turbulent entraining parcel simulations. *J. Atmos. Sci.*, **75**, 3365–3379, https://doi.org/10.1175/JAS-D-18-0078.1.

Baker, M. B., and J. Latham, 1979: The evolution of droplet spectra and the rate of production of embryonic raindrops in small cumulus clouds. *J. Atmos. Sci.*, **36**, 1612–1615, https://doi.org/10.1175/1520-0469(1979)036<1612:TEODSA>2.0.CO;2.

Beals, M., J. Fugal, R. Shaw, J. Lu, S. Spuler, and J. Stith, 2015: Holographic measurements of inhomogeneous cloud mixing at the centimeter scale. *Science*, **350**, 87–90, https://doi.org/10.1126/science.aab0751.

Bec, J., K. Gustavsson, and B. Mehlig, 2024: Statistical models for the dynamics of heavy particles in turbulence. *Annu. Rev. Fluid Mech.*, **56**, 189–213, https://doi.org/10.1146/annurev-fluid-032822-014140.

Bodenschatz, E., S. P. Malinowski, R. A. Shaw, and F. Stratmann, 2010: Can we understand clouds without turbulence? *Science*, **327**, 970–971, https://doi.org/10.1126/science.1185138.

Borghi, R., 1988: Turbulent combustion modelling. *Prog. Energy Combust. Sci.*, **14**, 245–292, https://doi.org/10.1016/0360-1285(88)90015-9.

Burnet, F., and J.-L. Brenguier, 2007: Observational study of the entrainment-mixing process in warm convective clouds. *J. Atmos. Sci.*, **64**, 1995–2011, https://doi.org/10.1175/JAS3928.1.

Chandrakar, K. K., W. Cantrell, S. Krueger, R. A. Shaw, and S. Wunsch, 2020: Supersaturation fluctuations in moist turbulent Rayleigh–Bénard convection: A two-scalar transport problem. *J. Fluid Mech.*, **884**, A19, https://doi.org/10.1017/jfm.2019.895.

——, W. W. Grabowski, H. Morrison, and G. H. Bryan, 2021: Impact of entrainment-mixing and turbulent fluctuations on droplet size distributions in a cumulus cloud: An investigation using Lagrangian microphysics with a sub-grid-scale model. *J. Atmos. Sci.*, **78**, 2983–3005, https://doi.org/10.1175/JAS-D-20-0281.1.

Chen, H., S. Chen, and R. Kraichnan, 1989: Probability distribution of a stochastically advected scalar field. *Phys. Rev. Lett.*, **63**, 2657–2660, https://doi.org/10.1103/PhysRevLett.63.2657.

Deardorff, J. W., 1980: Cloud top entrainment instability. *J. Atmos. Sci.*, **37**, 131–147, https://doi.org/10.1175/1520-0469(1980)037<0131:CTEI>2.0.CO;2.

Duplat, J., and E. Villermaux, 2008: Mixing by random stirring in confined mixtures. *J. Fluid Mech.*, **617**, 51–86, https://doi.org/10.1017/S0022112008003789.

Frezat, H., J. Le Sommer, R. Fablet, G. Balarac, and R. Lguensat, 2022: A posteriori learning for quasi-geostrophic turbulence parametrization. *J. Adv. Model. Earth Syst.*, **14**, e2022MS003124, https://doi.org/10.1029/2022MS003124.

Fries, J., G. Sardina, G. Svensson, and B. Mehlig, 2021: Key parameters for droplet evaporation and mixing at the cloud edge. *Quart. J. Roy. Meteor. Soc.*, **147**, 2160–2172, https://doi.org/10.1002/qj.4015.

——, ——, ——, A. Pumir, and B. Mehlig, 2023: Lagrangian supersaturation fluctuations at the cloud edge. *Phys. Rev. Lett.*, **131**, 254201, https://doi.org/10.1103/PhysRevLett.131.254201.

Grabowski, W. W., and G. C. Abade, 2017: Broadening of cloud droplet spectra through eddy hopping: Turbulent adiabatic parcel simulations. *J. Atmos. Sci.*, **74**, 1485–1493, https://doi.org/10.1175/JAS-D-17-0043.1.

Hoffmann, F., 2020: Effects of entrainment and mixing on the Wegener–Bergeron–Findeisen process. *J. Atmos. Sci.*, **77**, 2279–2296, https://doi.org/10.1175/JAS-D-19-0289.1.

——, 2023: The small-scale mixing of clouds with their environment: Impacts on micro-and macroscale cloud properties. *Clouds and their Climatic Impacts: Radiation, Circulation, and Precipitation*, S. C. Sullivan and C. Hoose, Eds., John Wiley and Sons, 255–270.

——, and G. Feingold, 2019: Entrainment and mixing in stratocumulus: Effects of a new explicit subgrid-scale scheme for large-eddy simulations with particle-based microphysics. *J. Atmos. Sci.*, **76**, 1955–1973, https://doi.org/10.1175/JAS-D-18-0318.1.

——, T. Yamaguchi, and G. Feingold, 2019: Inhomogeneous mixing in Lagrangian cloud models: Effects on the production of precipitation embryos. *J. Atmos. Sci.*, **76**, 113–133, https://doi.org/10.1175/JAS-D-18-0087.1.

Jakhar, K., Y. Guan, R. Mojgani, A. Chattopadhyay, and P. Hassanzadeh, 2024: Learning closed-form equations for subgrid-scale closures from high-fidelity data: Promises and challenges. *J. Adv. Model. Earth Syst.*, **16**, e2023MS003874, https://doi.org/10.1029/2023MS003874.

Kainz, J., and F. Hoffmann, 2023: The effects of aerosol on small-scale cloud-environment mixing: Implications for simulating and observing inhomogeneous mixing. *J. Geophys. Res. Atmos.*, **128**, e2023JD038509, https://doi.org/10.1029/2023JD038509.

——, M. Nikitabahen, N. B. Kumar, S. Ravichandran, J. Fries, G. Sardina, B. Mehlig, and F. Hoffmann, 2024: Benchmarking turbulence models to represent cloud-edge mixing. Zenodo, accessed 23 February 2026, https://doi.org/10.5281/zenodo.13813360.

Kerstein, A. R., 1988: A linear-eddy model of turbulent scalar transport and mixing. *Combust. Sci. Technol.*, **60**, 391–421, https://doi.org/10.1080/00102208808923995.

Krueger, S. K., 1993: Linear eddy modeling of entrainment and mixing in stratus clouds. *J. Atmos. Sci.*, **50**, 3078–3090, https://doi.org/10.1175/1520-0469(1993)050<3078:LEMOEA>2.0.CO;2.

——, and A. R. Kerstein, 2018: An economical model for simulating turbulence enhancement of droplet collisions and coalescence. *J. Adv. Model. Earth Syst.*, **10**, 1858–1881, https://doi.org/10.1029/2017MS001240.

——, C.-W. Su, and P. A. McMurtry, 1997: Modeling entrainment and finescale mixing in cumulus clouds. *J. Atmos. Sci.*, **54**, 2697–2712, https://doi.org/10.1175/1520-0469(1997)054<2697:MEAFMI>2.0.CO;2.

Kulmala, M., Ü. Rannik, E. L. Zapadinsky, and C. F. Clement, 1997: The effect of saturation fluctuations on droplet growth. *J. Aerosol Sci.*, **28**, 1395–1409, https://doi.org/10.1016/S0021-8502(97)00015-3.

Kumar, B., F. Janetzko, J. Schumacher, and R. A. Shaw, 2012: Extreme responses of a coupled scalar–particle system during turbulent mixing. *New J. Phys.*, **14**, 115020, https://doi.org/10.1088/1367-2630/14/11/115020.

——, J. Schumacher, and R. A. Shaw, 2013: Cloud microphysical effects of turbulent mixing and entrainment. *Theor. Comput. Fluid Dyn.*, **27**, 361–376, https://doi.org/10.1007/s00162-012-0272-z.

——, ——, and ——, 2014: Lagrangian mixing dynamics at the cloudy–clear air interface. *J. Atmos. Sci.*, **71**, 2564–2580, https://doi.org/10.1175/JAS-D-13-0294.1.

——, S. Bera, T. Parabhakaran, and W. W. Grabowski, 2017: Cloud-edge mixing: Direct numerical simulation and observations in Indian monsoon cloud. *J. Adv. Model. Earth Syst.*, **9**, 332–353, https://doi.org/10.1002/2016MS000731.

Lim, J.-S., and F. Hoffmann, 2024: Life cycle evolution of mixing in shallow cumulus clouds. *J. Geophys. Res. Atmos.*, **129**, e2023JD040393, https://doi.org/10.1029/2023JD040393.

Menon, S., and A. R. Kerstein, 2011: The Linear-Eddy Model. *Turbulent Combustion Modelling: Fluid Mechanics and Its Applications.* T. Echekki and E. Mastorakos, Eds., Springer Netherlands, 221–247, https://doi.org/10.1007/978-94-007-0412-1_10.

Moin, P., and K. Mahesh, 1998: Direct numerical simulation: A tool in turbulence research. *Annu. Rev. Fluid Mech.*, **30**, 539–578, https://doi.org/10.1146/annurev.fluid.30.1.539.

Pope, S., 1991: Mapping closures for turbulent mixing and reaction. *Theor. Comput. Fluid Dyn.*, **2**, 255–270, https://doi.org/10.1007/BF00271466.

——, 1994: Lagrangian PDF methods for turbulent flows. *Annu. Rev. Fluid Mech.*, **26**, 23–63, https://doi.org/10.1146/annurev.fl.26.010194.000323.

——, 2000: *Turbulent Flows.* Cambridge University Press, 771 pp.

——, 2011: Simple models of turbulent flows. *Phys. Fluids*, **23**, 011301, https://doi.org/10.1063/1.3531744.

Pozorski, J., and M. Waclawczyk, 2020: Mixing in turbulent flows: An overview of physics and modelling. *Processes*, **8**, 1379, https://doi.org/10.3390/pr8111379.

Rogers, R. R., and M. K. Yau, 1989: *A Short Course in Cloud Physics.* 3rd ed. Butterworth-Heinemann, 302 pp.

Saito, I., T. Watanabe, and T. Gotoh, 2021: Statistical properties of a stochastic model of eddy hopping. *Atmos. Chem. Phys.*, **21**, 13 119–13 130, https://doi.org/10.5194/acp-21-13119-2021.

Smagorinsky, J., 1963: General circulation experiments with the primitive equations. *Mon. Wea. Rev.*, **91**, 99–164, https://doi.org/10.1175/1520-0493(1963)091<0099:GCEWTP>2.3.CO;2.

Thomas, S., P. Prabhakaran, W. Cantrell, and R. A. Shaw, 2021: Is the water vapor supersaturation distribution Gaussian? *J. Atmos. Sci.*, **78**, 2385–2395, https://doi.org/10.1175/JAS-D-20-0388.1.

Vaillancourt, P., M. Yau, and W. W. Grabowski, 2001: Microscopic approach to cloud droplet growth by condensation. Part I: Model description and results without turbulence. *J. Atmos. Sci.*, **58**, 1945–1964, https://doi.org/10.1175/1520-0469(2001)058<1945:MATCDG>2.0.CO;2.

Villermaux, E., and J. Duplat, 2003: Mixing as an aggregation process. *Phys. Rev. Lett.*, **91**, 184501, https://doi.org/10.1103/PhysRevLett.91.184501.

Villermaux, J., 1986: Micromixing phenomena in stirred reactors. *Encyclopedia of Fluid Mechanics*, Vol. 2, N. P. Cheremisinoff Eds., Gulf Publishing Company, 707–771.